Applied Catalysis B: Environment and Energy 402 (2027) 127409

Contents lists available at ScienceDirect

Applied Catalysis B: Environment and Energy

journal homepage: www.elsevier.com/locate/apcatb

Interfacial engineering of COF-TpBpy/CdSe S-scheme heterojunction for robust H_2O_2 photocatalytic production

Mohan Zhang [a], Yu Zhang [a], Jiayi Meng [a], Jiajie Wang [b], Jiaqi Du [b], Hongwei Chen [b], Yifan Liao [a], Yuchen Wei [a], Quanmei Zhou [a], Yuying Hu [a], Yakun Song [a], Hongyan Zhao [a], Wei-Lin Dai [a,*]

[a] State Key Laboratory of Porous Materials for Separation and Conversion, Shanghai Key Laboratory of Molecular Catalysis and Innovative Materials, Department of Chemistry, Fudan University, Shanghai, 200438, PR China

[b] State Key Laboratory of Porous Materials for Separation and Conversion, Southwest Research & Design Institute of the Chemical Industry, Chengdu, 610225, PR China

ARTICLE INFO

Keywords:
Interfacial engineering
S-Scheme mechanism
COF based composites
CdSe heterojunction
Photocatalytic H_2O_2 production

ABSTRACT

Photocatalytic H_2O_2 production via oxygen reduction represents a sustainable pathway for solar-to-chemical energy conversion. However, constructing sacrificial-agent-free heterojunctions that simultaneously maximize charge separation and preserve redox ability remains a significant challenge. Herein, we report a molecular-level interfacial engineering strategy to anchor COF-TpBpy onto CdSe nanorods via *in-situ* solvothermal growth, fabricating a strongly coupled organic–inorganic S-scheme heterojunction. Benefiting from the intimate interfacial contact, the optimized 10CdSe/TpBpy composite achieves a remarkable H_2O_2 yield of 4349 $\mu mol \cdot g^{-1} \cdot h^{-1}$ in pure water without any sacrificial agents, alongside an impressive apparent quantum yield (AQY) of 11.1% at 450 nm. Mechanistic investigations, combining Density Functional Theory (DFT) calculations, Kelvin probe force microscopy (KPFM), and *in-situ* irradiated X-ray photoelectron spectroscopy (*in-situ* XPS), visually confirm a robust built-in internal electric field (IEF) driven by the work function difference. Furthermore, femtosecond transient absorption (fs-TA) spectroscopy reveals an ultrafast picosecond-scale interfacial charge transfer behavior, providing direct kinetic evidence for the S-scheme mechanism. This unique charge transfer pathway effectively preserves the strong reducing electrons in the CdSe conduction band to boost the oxygen reduction reaction (ORR) kinetics. This work offers a viable paradigm for designing robust hybrid S-scheme architectures for efficient photocatalysis.

1. Introduction

Hydrogen peroxide (H_2O_2) is a green, environmentally friendly chemical product widely used in chemical, medical, and other fields, with a continuously growing global demand [1–3]. The current mainstream H_2O_2 production method is the anthraquinone process, which involves complex steps [4] and, more importantly, generates various organic wastes that cause environmental issues [5]. Among numerous clean production technologies, photocatalytic H_2O_2 synthesis has shown immense application potential due to its green process and mild operating conditions [6,7]. Nonetheless, conventional single-component photocatalytic systems typically face the drawback of rapid electron-hole pair recombination upon photoexcitation, meaning the absorbed light energy is mostly consumed through radiative or non-radiative pathways [8]. Therefore, synthesizing heterostructured photocatalysts with enhanced charge separation efficiency has become a focal point for researchers [9].

Constructing S-scheme heterojunctions with highly efficient charge separation capabilities has been a primary research focus in photocatalytic material design in recent years [10]. Generally, an S-scheme heterojunction is composed of a reduction photocatalyst (RP) and an oxidation photocatalyst (OP). Upon physical contact, interfacial recombination occurs between the conduction band (CB) electrons of the OP and the valence band (VB) holes of the RP [11]. Such a charge-transfer pathway intentionally retains the highly reductive electrons within the RP's CB and the highly oxidative holes within the OP's VB, which concurrently optimizes the overall redox capability and ensures efficient charge separation [12–14]. Integrating

* Corresponding author.
E-mail address: wldai@fudan.edu.cn (W.-L. Dai).

https://doi.org/10.1016/j.apcatb.2026.127409
Received 15 July 2026; Received in revised form 22 August 2026; Accepted 27 August 2026
Available online 29 August 2026

multi-energy-state covalent organic frameworks with metal compound has proven highly effective in bridging interfacial charge transfer while preserving robust redox potentials for exceptional H_2O_2 generation [15,16]. Similarly, integrating metal solid-solutions with polymeric scaffolds significantly broadens light harvesting and enriches active surface sites [17,18]. Nevertheless, the construction of most current S-scheme heterojunctions relies on simple physical mixing or electrostatic self-assembly. These approaches inevitably lead to loose interfacial contact and abundant interfacial defects, failing to establish a sufficiently strong internal electric field to drive rapid charge transfer, which severely masks the true potential of the S-scheme mechanism. Consequently, constructing a strongly coupled interface between energy-band-matched semiconductors via molecular-level interfacial engineering, and deciphering its dynamic charge transfer mechanism at the atomic/molecular scale, remains a formidable challenge.

Complementary organic/inorganic semiconductor heterojunctions present an ideal platform to mitigate the aforementioned limitations [19–22]. As an important semiconductor material, CdSe possesses a relatively narrow bandgap (approximately 1.7 eV), enabling it to absorb photons over a broad visible light region to generate photogenerated electrons and holes [9,23–25]. However, CdSe is plagued by a fast recombination rate of photogenerated carriers [26], and a susceptibility to photocorrosion, which limits its structural stability in practical applications [27]. Conversely, covalent organic frameworks (COFs), as an exemplary category of porous organic materials linked by covalent bonds, possess high crystallinity, large π-conjugated structures, and abundant active sites, exhibiting extraordinary photocatalytic potential [28–30]. Specifically, the bipyridine-functionalized COF-TpBpy not only demonstrates excellent chemical stability, but its skeleton also possesses electron-rich nitrogen atoms, which have a natural propensity to form strong interactions with metal sites. The staggered band alignment between CdSe and COF-TpBpy provides a perfect physicochemical and thermodynamic prerequisite for forming a robust internal electric field. A chemically coupled integration of these two materials is expected to simultaneously overcome the photocorrosion of CdSe and maximize the catalytic activity of the COF material [31–33].

Herein, we developed an in situ solvothermal growth method to facilely anchor COF-TpBpy materials onto CdSe nanorods. This in situ growth strategy enables the formation of a tightly coupled interface with strong electronic interactions, thereby establishing an exceedingly powerful internal electric field directed from CdSe to COF-TpBpy. When tested in pure water absent of sacrificial electron donors, the best-performing 10CdSe/TpBpy hybrid delivered a remarkable H_2O_2 evolution rate reaching 4349 $\mu mol \cdot g^{-1} \cdot h^{-1}$, which vastly exceeds the activities of its isolated constituents. More importantly, we comprehensively elucidated the S-scheme carrier migration route and the dual-channel reaction mechanism through multi-dimensional characterizations. DFT, Kelvin probe force microscopy (KPFM) and in-situ light irradiation X-ray photoelectron spectroscopy (in-situ XPS) explicitly visualized the robust built-in internal electric field (IEF) and interfacial band bending, while femtosecond transient absorption (fs-TA) spectroscopy provided kinetic proof of the ultrafast S-scheme charge recombination. This study not only presents a highly competitive catalyst system for green H_2O_2 synthesis, but also provides profound mechanistic insights for designing high-performance organic-inorganic hybrid S-scheme heterojunctions for advanced solar energy conversion.

2. Experimental section

2.1. Materials

5,5′-Diamino-2,2′-bipyridine (Bpy, ≥ 97%), cadmium chloride ($CdCl_2 \cdot 2.5\ H_2O$, AR), and N,N-dimethylacetamide (DMAc, ≥ 99.8%) were purchased from Aladdin Bio-Chem Technology Co., Ltd. 1,3,5-Triformylphloroglucinol (Tp, ≥ 97%), aqueous acetic acid (36%), and o-dichlorobenzene (o-DCB, ≥ 98.0%) were purchased from Shanghai Maclin Biochemical Technology Co., Ltd. Selenium powder (≥ 98.0%), diethylenetriamine (DETA, ≥ 99.99%), and hydrazine hydrate ($N_2H_4 \cdot H_2O$, 50%) were purchased from Sinopharm Chemical Reagent Co., Ltd. Deionized (DI) water and ethanol (C_2H_5OH, AR) were used as received without further purification.

2.2. Synthesis of CdSe

The precursor mixture was prepared by introducing 1 mmol Se powder and 1 mmol $CdCl_2 \cdot H_2O$ into a 100 mL PTFE vessel, followed by the sequential addition of deionized water (6 mL), $N_2H_4 \cdot H_2O$ (12 mL), and DETA (18 mL). This combination underwent magnetic agitation for 15 min to guarantee complete blending. Afterward, the suspension was kept under constant stirring at ambient conditions for another 60 min, facilitating an even distribution of all components. The resulting liquid was then sealed within a stainless-steel solvothermal reactor (100 mL) and thermally treated at 100 °C over a 12-hour period. Then centrifugal separation was utilized to harvest the solid products. Any residual byproducts or unreacted species were eliminated by rinsing the recovered solids iteratively, applying ethanol alongside pure water for three consecutive cycles. Ultimately, pristine CdSe nanorods were acquired following an 18-hour lyophilization process.

2.3. Synthesis of COF-TpBpy

The fabrication of COF-TpBpy relied on a standard Schiff-base coupling reaction [34]. First, 5,5′-diamino-2,2′-bipyridine (Bpy, 41.9 mg), 1,3,5-triformylphloroglucinol (Tp, 31.5 mg), N, N-dimethylacetamide (DMAc, 2.25 mL), and o-dichlorobenzene (o-DCB, 0.75 mL) were added into a Pyrex tube and ultrasonically dispersed. Subsequently, 0.3 mL of aqueous acetic acid (6 M concentration) was swiftly injected into this suspension. The system underwent a rigorous freeze-pump-thaw procedure repeated three times, before being subjected to a 72-hour heating step at 120 °C. The distinct red powder yielded from this process was purified by successive washings employing acetone, dichloromethane, as well as DMAc, and then was collected after overnight desiccation in a 150 °C vacuum oven.

2.4. Preparation of CdSe/TpBpy

The CdSe/COF-TpBpy composite materials were synthesized via an in situ solvothermal method. Following ultrasonic dispersion, the process was identical to the aforementioned COF-TpBpy synthesis. Prior to sonication, pre-prepared CdSe nanorod powder was added to the mixture. Composites with different CdSe proportions were prepared by varying the mass of the added CdSe powder. For ease of comparison, the composites containing different masses of CdSe are denoted as xCdSe/TpBpy (x = 2, 5, 10, 15, 30, 50), where "x" represents the mass ratio of CdSe to COF-TpBpy.

2.5. Characterization and theoretical method

The apparatus for the characterization and the computational details can be found in the Supporting Information.

3. Results and discussion

3.1. Synthesis and characterization of CdSe@COF-TpBpy catalysts

The CdSe/TpBpy heterojunction photocatalyst was synthesized via an in situ solvothermal growth mechanism, as illustrated in Fig. 1a. First, highly crystalline CdSe nanorods were pre-synthesized via a solvothermal method, and their surfaces provided attachment interfaces for the growth of the COF. Under the catalysis of 36% acetic acid, the aldehyde groups of Tp and the amino groups of Bpy underwent a typical Schiff base condensation reaction [35]. The newly generated

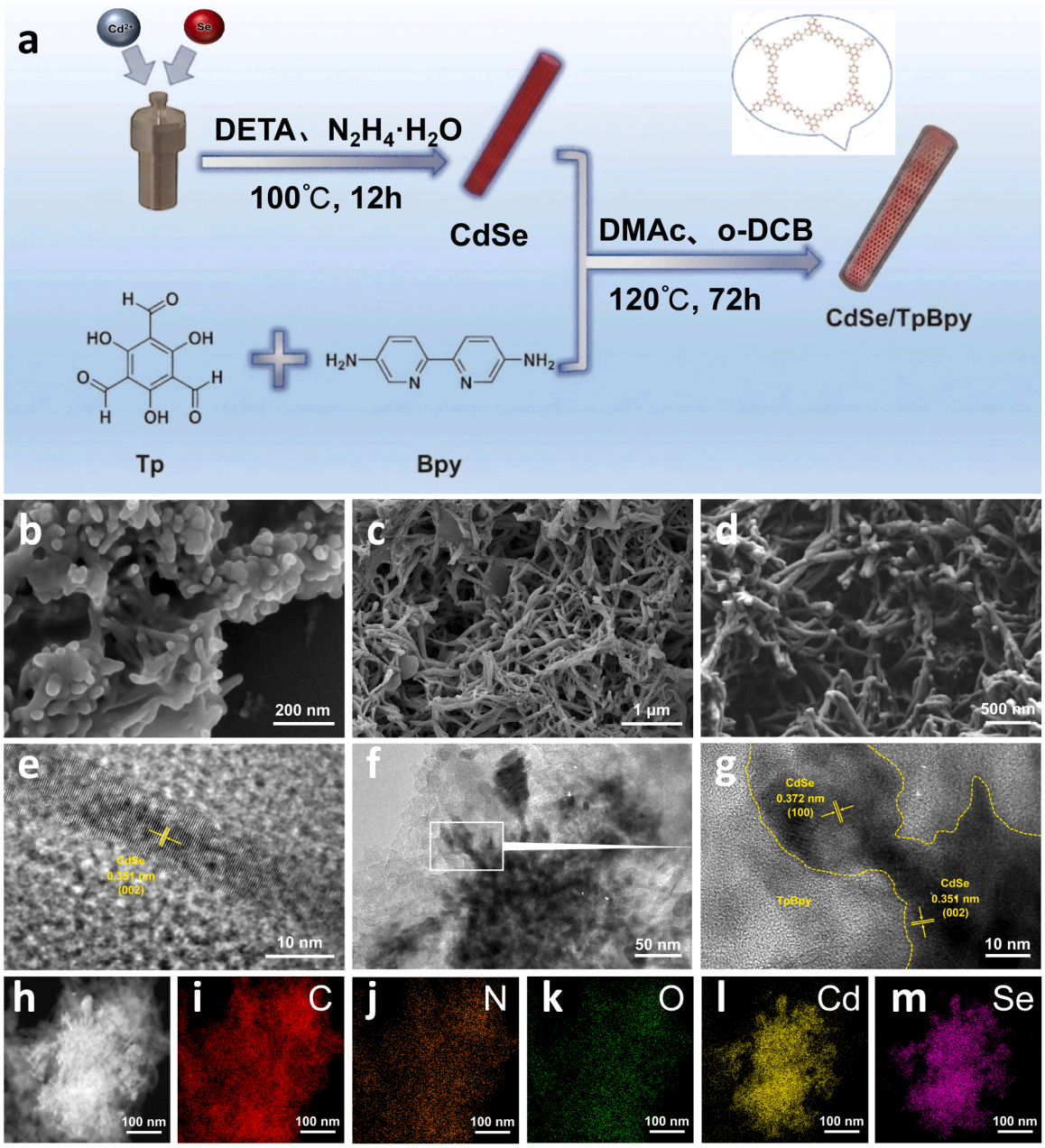

Fig. 1. (a) Synthetic route of CdSe/TpBpy. SEM images of (b) CdSe, (c) COF-TpBpy, and (d) CdSe/TpBpy. (e) HRTEM image of CdSe. (f) TEM and (g) HRTEM images of CdSe/TpBpy. (h-m) EDX mappings of C, N, O, Cd, and Se elements in CdSe/TpBpy.

COF-TpBpy nucleated in situ on the surface of CdSe, forming a reticular structure in close contact with the nanorods, thus constructing the heterostructure. The morphology and three-dimensional spatial topology of the samples was investigated by scanning electron microscopy (SEM), transmission electron microscopy (TEM) and atomic force microscopy (AFM). The CdSe exhibited a nanorod morphology (Fig. 1b, S1a), while the pure COF-TpBpy displayed an interconnected network structure assembled from nanowires (Fig. 1c, S1b). After compounding, the CdSe/TpBpy composite significantly retained the nanowire network of the COF (Fig. 1d), and the TEM image of CdSe/TpBpy demonstrated a distinct phase boundary between the two components (Fig. 1f-g). High-resolution TEM (HRTEM) analysis of a selected rectangular area revealed that compared with CdSe (Fig. 1e), the (002) lattice spacing of CdSe in the composite remained 0.351 nm, indicating that COF-TpBpy was effectively encapsulated on the CdSe surface. Furthermore, energy-dispersive X-ray spectroscopy (EDS) elemental mapping (Fig. 1h-m) confirmed the uniform distribution of Cd, Se, C, N, and O throughout the composite architecture. The AFM results show that both CdSe and the CdSe/TpBpy composite (Fig. S2a, S2c) exhibit surface height of approximately 300 nm while the pure COF-TpBpy was around 200 nm (Fig. S2b).

To evaluate the crystallographic properties of all synthesized materials, X-ray diffraction (XRD) measurements were utilized. As shown in Fig. 2a, pure COF-TpBpy displays an intense signal located at a low angle of 3.6°, which corresponds to the open channels' (100) crystalline plane. The CdSe sample displays multiple sharp diffraction peaks at 23.9°, 25.4°, 27.1°, 42.0°, 45.8°, and 49.7°, perfectly matching the (100), (002), (101), (110), (103), and (112) planes of wurtzite CdSe (JCPDS No. 08–0459). Regarding the engineered xCdSe/TpBpy heterostructures, elevating the inorganic precursor amount progressively amplifies the intensity of cadmium selenide-related signals, simultaneously causing a proportional decline in the organic framework's diffraction

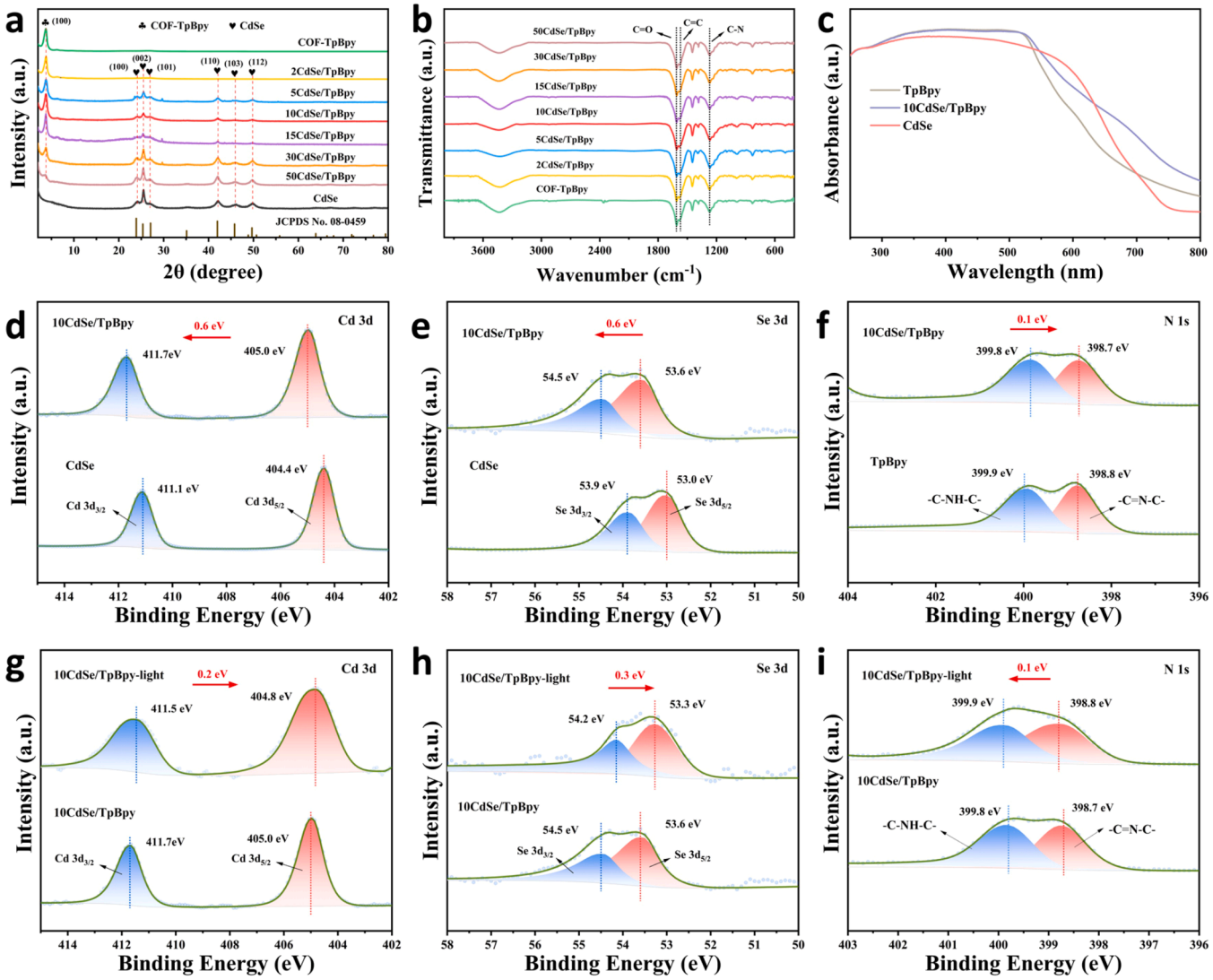

Fig. 2. (a) XRD profiles of the fabricated materials. (b) FT-IR spectra comparing the respective samples. (c) UV-Vis diffuse reflectance spectra of the photocatalysts. Ex situ and in situ light-irradiation high-resolution XPS spectra of (d,g) Cd 3d, (e,h) Se 3d and (f,i) N 1 s in CdSe, COF-TpBpy and 10CdSe/TpBpy.

intensity. Identification of the present chemical moieties was subsequently accomplished utilizing Fourier transform infrared (FT-IR) evaluations (Fig. 2b). Both pristine COF-TpBpy and xCdSe/TpBpy showed strong characteristic peaks at 1608 cm^{-1} and 1579 cm^{-1} for C═O and C═C groups, corresponding to keto stretching frequencies. Furthermore, detection of an additional signal near 1268 cm^{-1} confirms the existence of C-N bonds. Notably, the xCdSe/TpBpy composites exhibited almost identical characteristic peaks to pristine COF-TpBpy, indicating that the integration of CdSe nanorods did not disrupt the molecular skeleton of the COF. As shown in the UV-Vis DRS spectra (Fig. 2c), the integration of CdSe effectively broadens the spectral response, maximizing the light-harvesting capacity of the photocatalyst. Comprehensive investigations regarding superficial elemental makeup alongside interfacial charge dynamics were carried out applying XPS. Survey scan focusing on the 10CdSe/TpBpy verified the simultaneous presence of O, N, C, Se, and Cd elements (Fig. S3). Fine-scan evaluations underwent energy calibration relying upon the standard adventitious C 1 s signal located at 284.8 eV (Fig. S4a). Upon the formation of the 10CdSe/TpBpy heterojunction, the Cd 3d and Se 3d peaks shift significantly toward higher binding energies by 0.6 eV compared to pristine CdSe (Fig. 2d-e) [9,36]. Conversely, the N 1 s and O 1 s peaks of TpBpy (Fig. 2 f, S4b) [37] shift to a lower binding energy by 0.1 eV. These opposite shifts unambiguously demonstrate that electrons flow toward the covalent organic framework upon contact, establishing a robust IEF directed from CdSe to TpBpy.

To precisely investigate the charge transfer mechanism under working conditions, high-resolution in situ irradiated XPS measurements were conducted. Under visible light irradiation, the binding energies of Cd 3d and Se 3d in 10CdSe/TpBpy shifted negatively by 0.2 eV and 0.3 eV, respectively (Fig. 2g-h), while the N 1 s peak shifted positively by 0.1 eV (Fig. 2i). This light-induced reverse shift verifies that, driven by the IEF, the photogenerated electrons in the conduction band of TpBpy migrate to the valence band of CdSe for recombination. These results provide solid evidence for the S-scheme charge-transfer pathway.

Porosity characteristics and surface area parameters of these synthesized materials were determined via nitrogen physisorption measurements. Both pure COF-TpBpy and the 10CdSe/TpBpy composite displayed typical Type IV isotherms (Fig. S5), indicative of mesoporous or microporous structures. According to Brunauer-Emmett-Teller (BET) calculations, the COF-TpBpy achieved an impressive geometric footprint reaching 1112 m^2/g, accompanied by 0.6 cm^3/g regarding overall cavity volume (Table 1). Furthermore, the pore size distribution curves (Fig. S6) revealed that the pore sizes of COF-TpBpy and the 10CdSe/TpBpy composite are centered similarly at approximately 1.6 nm and 1.7 nm, respectively. This finding confirms that the intrinsic porous skeleton of the COF was well preserved after integration. Pure CdSe

Table 1
Specific surface area (S_{BET}), pore size (D_{pore}), and pore volume (V_{pore}) for CdSe, COF-TpBpy, and 10CdSe/TpBpy.

Sample	S_{BET} (m^2/g)	D_{pore} (nm)	V_{pore} (cm^3/g)
CdSe	106	33.7	0.5
COF-TpBpy	1112	1.6	0.6
10CdSe/TpBpy	523	1.7	0.4

displayed a broad pore size distribution centered at 33.7 nm, likely stemming from interstitial voids formed between stacked nanorods. Despite the overall decrease in specific surface area, the well-preserved microporous/mesoporous channels in 10CdSe/TpBpy remain highly advantageous for the adsorption of reactants and rapid diffusion of products during the photocatalytic process.

3.2. Photophysical characteristics and electrochemical assessments

Dynamics concerning carrier dissociation plus subsequent mobilization underwent rigorous scrutiny utilizing transient photocurrent evaluations coupled with electrochemical impedance spectroscopy (EIS). The EIS Nyquist plots revealed that the 10CdSe/TpBpy composite possessed the smallest arc radius (Fig. 3a), which reduced electrical resistance at the material boundary, thereby accelerating interfacial carrier transport kinetics. Additionally, compared with pure CdSe and COF-TpBpy, the 10CdSe/TpBpy composite exhibited a significantly enhanced photocurrent density under visible light irradiation (Fig. 3b), providing direct evidence of its high photoelectric conversion efficiency. Photoluminescence (PL) and time-resolved photoluminescence (TRPL) spectra were employed to elucidate charge recombination behaviors. Compared with pure COF-TpBpy, the PL emission intensity of 10CdSe/TpBpy was significantly quenched (Fig. 3c), which serves as robust evidence indicating substantial suppression of detrimental electron-hole recombination events. The TRPL decay curves of both samples were perfectly fitted using a bi-exponential decay model (Fig. 3d). For the pure COF-TpBpy, the fluorescence decay process consists of a fast decay component ($\tau_1 = 0.187$ ns) and a slow decay component ($\tau_2 = 1.018$ ns), yielding a calculated average fluorescence lifetime (τ_{ave}) of 0.33 ns. In contrast, upon the introduction of CdSe to construct a heterojunction, the 10CdSe/TpBpy composite exhibits a noticeably accelerated fluorescence decay dynamic, with its time constants τ_1 and τ_2 changing to 0.158 ns and 1.027 ns, respectively, leading to a shortened overall average lifetime of 0.31 ns. The quenching and shortening of the fluorescence lifetime in the composite provide strong kinetic evidence for the existence of an efficient non-radiative charge transfer pathway at the heterojunction interface formed between CdSe and COF-TpBpy [9,38]. Light-harvesting capabilities alongside corresponding energy-band configurations were investigated employing ultraviolet-visible diffuse reflectance spectroscopy (UV-Vis DRS). According to the Tauc plots (Fig. S7c-d), the bandgap energy of pristine CdSe was calculated as 1.83 eV, narrower than that of pristine COF-TpBpy (2.08 eV). Furthermore, Mott-Schottky measurements were conducted to determine the relative band positions. Pristine CdSe yielded a flat-band potential situated around −1.19 V (vs. NHE, Fig. S7b). Considering its nature as an n-type semiconductor material, this measured flat-band value virtually

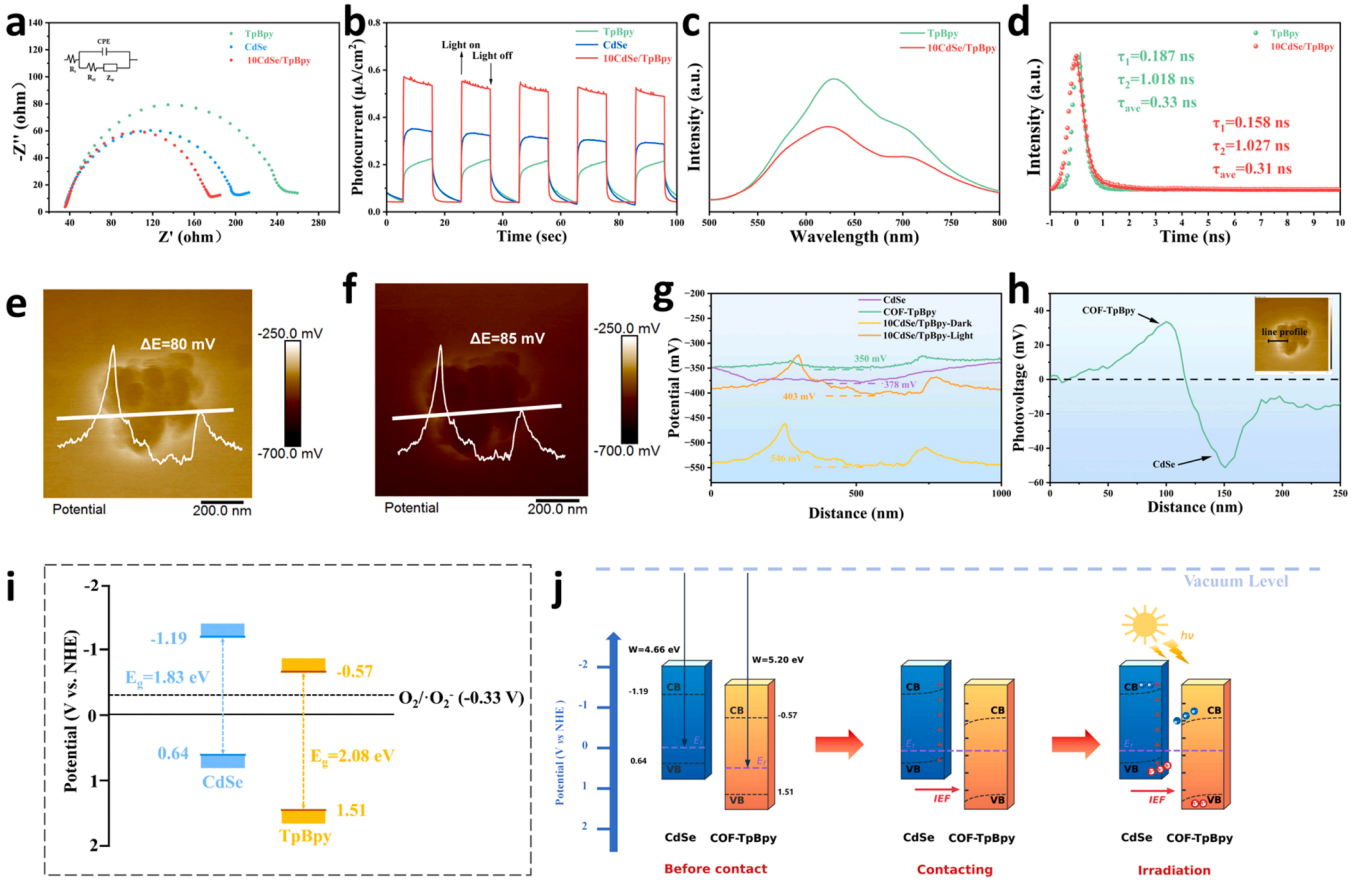

Fig. 3. (a) EIS Nyquist plots and (b) Photocurrent responses of CdSe, COF-TpBpy, and 10CdSe/TpBpy. (c) PL spectra and (d) TRPL decay spectra of COF-TpBpy and 10CdSe/TpBpy. KPFM surface potential maps and corresponding line profiles of the 10CdSe/TpBpy composite under (e) dark and (f) illumination conditions. (g) Surface potential line profiles of CdSe, COF-TpBpy, and 10CdSe/TpBpy in the dark and under illumination. (h) The corresponding surface photovoltage (SPV) line profile of 10CdSe/TpBpy. The inset displays the line profile scanning path. (i) Schematic illustration of the band structures for CdSe and COF-TpBpy. (j) Schematic illustration of charge transfer in the CdSe/TpBpy S-scheme heterojunction.

mirrors its conduction band minimum (E_{CB}). Utilizing the fundamental relationship $E_g = E_{VB} - E_{CB}$, the corresponding valence band maximum (E_{VB}) for this inorganic phase was deduced as 0.64 V. Concurrently, referencing established prior characterizations (Fig. S7a), the E_{CB} alongside E_{VB} for the COF-TpBpy were identified at −0.57 V plus 1.46 V (vs. NHE), respectively. Based on these results, the staggered band alignment of CdSe and COF-TpBpy is depicted (Fig. 3i), which creates a favorable potential gradient for the transfer of photogenerated electrons from the conduction band of CdSe to the conduction band of COF-TpBpy, whose energy levels perfectly satisfy the thermodynamic requirements for the photocatalytic reduction of O_2 to $\cdot O_2^-$ [39,40].

To spatially visualize the interfacial charge transfer behavior and the distribution of IEF at the nanoscale, KPFM measurements were conducted. As depicted in Fig. S8 (a-b), pristine CdSe exhibits a higher surface potential than pure TpBpy, indicating a smaller work function and a higher Fermi level for CdSe. Given the core-shell-like architecture where COF-TpBpy wraps around CdSe, the potential profile clearly reveals a higher potential in the central region (CdSe) and a lower potential at the edge layer (TpBpy) (Fig. 3e,g). This result visually confirms the establishment of a robust IEF directed from CdSe to COF-TpBpy.

Under visible-light illumination, the overall surface potential of the composite significantly increases (Fig. 3f,g), and the interfacial potential difference enlarges from 80 mV to 85 mV. To precisely track the spatial distribution of photogenerated carriers, the surface photovoltage profile was extracted (Fig. 3h). The SPV profile demonstrates a positive signal in the outer COF-TpBpy region and a negative signal in the inner CdSe region. This crucial phenomenon indicates that, driven by the IEF, photogenerated electrons in the conduction band of TpBpy directionally migrate to the valence band of CdSe for recombination. Thus, a massive amount of positively charged holes accumulates on the TpBpy (yielding SPV > 0), while electrons are optimally retained in the CdSe (yielding SPV < 0) [41]. This spatial evolution of charges perfectly aligns with the thermodynamic deductions of the band structures and accords well with the light-induced reverse binding energy shifts observed in the *in-situ* light-irradiation XPS. Collectively, these results imply the robust S-scheme charge-transfer mechanism in the CdSe/TpBpy heterojunction (Fig. 3j).

The ultrafast dynamics of photogenerated carriers were investigated using femtosecond transient absorption (fs-TA) spectroscopy. Upon visible-light pumping, the ground-state bleaching (GSB) signal of COF-TpBpy is primarily located at shorter wavelengths (Fig. 4a,d), whereas the 10CdSe/TpBpy exhibits a prominent negative GSB signal in the 600–700 nm range (Fig. 4b,e). This newly emerged absorption band corresponds to the intrinsic excitonic transition of the narrower-bandgap CdSe, which indicates strong electronic coupling at the heterojunction interface. COF-TpBpy follows a bi-exponential decay, while the composite transitions to a tri-exponential mode (Fig. 4c,f). In both materials, the fast component τ_1 is assigned to hot-carrier shallow defect trapping and the shortened τ_1 in 10CdSe/TpBpy suggests a higher density of interfacial trapping sites. The slow component (τ_2 in TpBpy and τ_3 in the composite) represents intrinsic electron-hole radiative recombination. Notably, a new intermediate component τ_2 (3.23 ps) emerges in 10CdSe/TpBpy, which provides direct kinetic evidence for the S-scheme directional charge recombination. The decrease in overall lifetime was considered to originate from the additional recombination channel introduced by the S-scheme mechanism.

3.3. Evaluation of photocatalytic H_2O_2 synthesis and photocatalytic mechanism

Assessments regarding the visible-light-driven ($\lambda \geq 420$ nm) generation of hydrogen peroxide were conducted using purely aqueous media without adding any sacrificial agents. As shown in Fig. 5a, the H_2O_2 production rate of pristine CdSe was extremely low, at only 523 $\mu mol \cdot g^{-1} \cdot h^{-1}$, likely due to severe charge recombination [26]. Pure COF-TpBpy displayed a moderate rate of 1794 $\mu mol \cdot g^{-1} \cdot h^{-1}$. However, the composite significantly enhanced the catalytic activity, achieving a maximum H_2O_2 yield of 4349 $\mu mol \cdot g^{-1} \cdot h^{-1}$, which outpaces the CdSe alongside COF-TpBpy by factors of roughly 9.3 and 2.4. This extraordinary enhancement is primarily attributed to the synergistic effect of the heterojunction, which provides abundant active sites and accelerates charge separation while retaining strong redox capability.

Nevertheless, further increasing the CdSe content beyond the optimal ratio led to a slight decline in activity, which could be attributed to the shielding effect and excessive self-aggregation of CdSe nanorods hindering light harvesting and blocking active sites [52]. To gain deeper

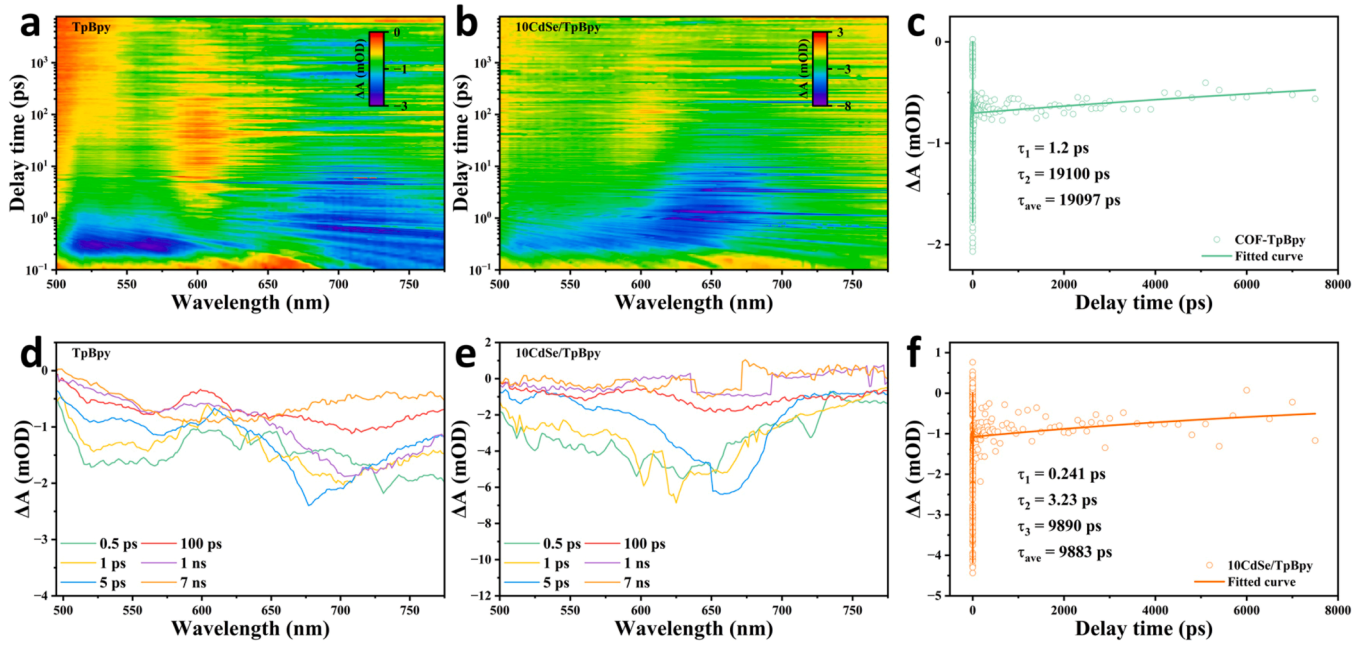

Fig. 4. Two-dimensional pseudocolor contour plots of the femtosecond transient absorption (fs-TA) spectra for (a) COF-TpBpy and (b) 10CdSe/TpBpy. The fs-TA spectra at indicated delay times for (d) COF-TpBpy and (e) 10CdSe/TpBpy. Transient absorption decay kinetics and the corresponding multi-exponential fitting curves for (c) TpBpy and (f) 10CdSe/TpBpy.

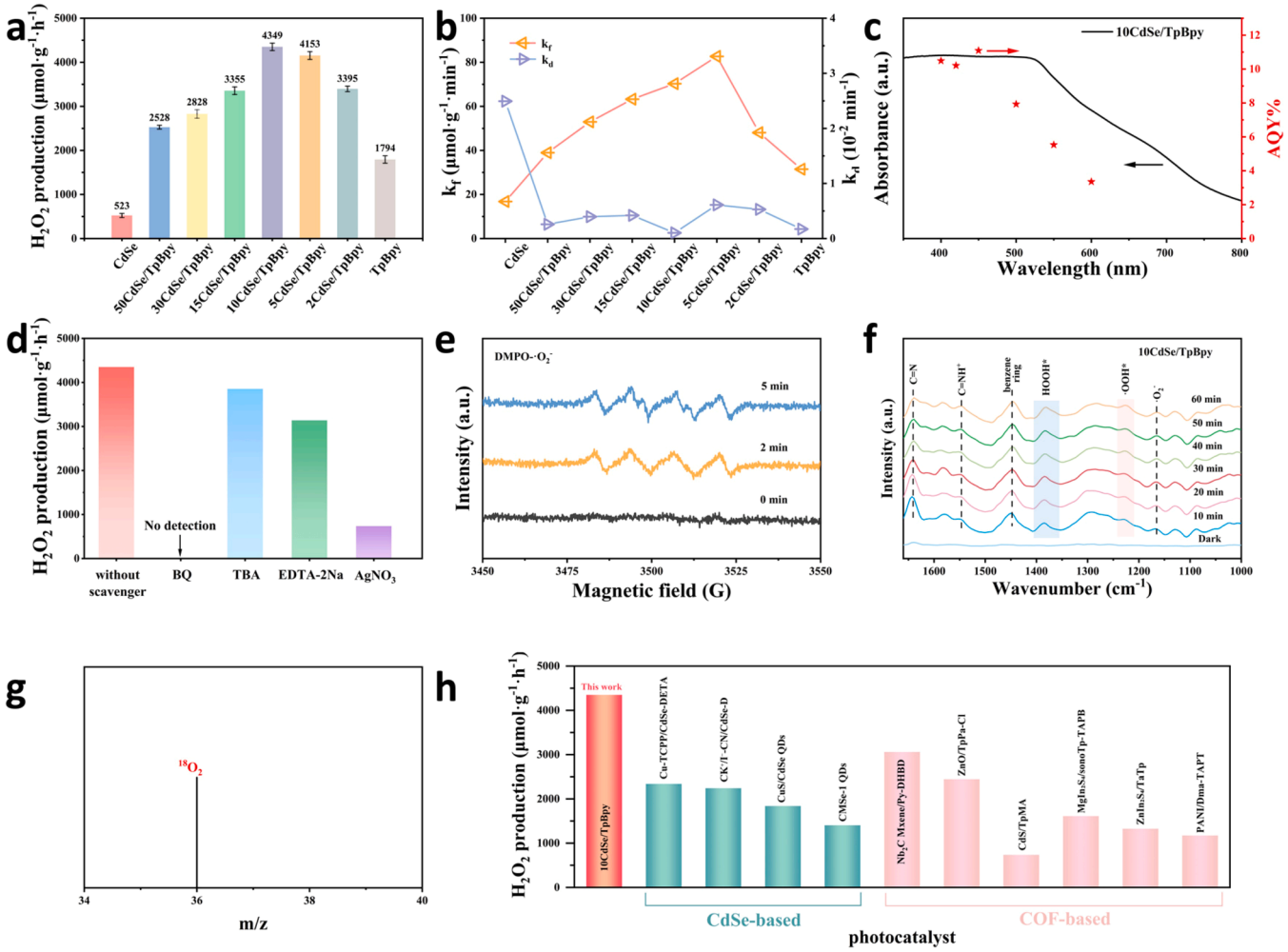

Fig. 5. (a) H_2O_2 production rates under visible light irradiation in pure water and air. (b) K_f and K_d of photocatalytic H_2O_2 production. (c) Apparent quantum yield. (d) Photocatalytic H_2O_2 production rates of 10CdSe/TpBpy with different scavengers (BQ, TBA, EDTA-2Na, $AgNO_3$). (e) EPR spectra of DMPO-·O_2^- over 10CdSe/TpBpy at 0, 2, and 5 min. (f) In situ FT-IR spectra of 10CdSe/TpBpy for photocatalytic H_2O_2 production. (g) The SIM spectrum of mass spectrum of the isotope tracing experiment using $^{18}O_2$. (h) Photocatalytic H_2O_2 production rates of various reported photocatalysts [35,42–51].

insights into the reaction kinetics, the formation (K_f) and decomposition (K_d) rate constants were systematically calculated (Fig. 5b). It was found that COF-TpBpy had a low K_f (31.5 μmol·g^{-1}·min^{-1}) and a higher K_d (0.002 min^{-1}). In sharp contrast, its composite with CdSe exhibited a high K_f (70.3 μmol·g^{-1}·min^{-1}) and the lowest K_d (0.001 min^{-1}), proving that the composite structure not only significantly promotes H_2O_2 generation but also effectively suppresses its rapid decomposition. Stability is a critical indicator for the practical application of photocatalysts. Stability tests for H_2O_2 production were conducted over 8 h. As shown in Fig. S9, the composite exhibited excellent stability during the initial 4 h with only a minor decay in the H_2O_2 yield. After undergoing 8 h of rigorous testing, the catalyst still maintained a high activity. Moreover, compared with the freshly prepared sample, the XRD pattern, XPS and TEM image of the used photocatalyst indicated no obvious changes (Fig. S10), highlighting the superior structural and chemical durability of this composite during long-term photocatalytic processes. Furthermore, the apparent quantum yield (AQY) of 10CdSe/TpBpy was measured under various monochromatic wavelengths. As depicted in Fig. 5c, the AQY action spectrum closely matches its UV-Vis absorption spectrum, reaching a remarkable maximum of 11.1% at 450 nm. This matching trend explicitly confirms that the H_2O_2 production process is inherently driven by the incident photons. Fig. 5h and Table S1 present a performance comparison with other CdSe-based and COF-based heterojunction photocatalysts, indicating that 10CdSe/TpBpy possesses highly satisfactory photocatalytic activity.

Unraveling the fundamental light-driven reaction routes necessitated conducting radical scavenging assays on our synthesized materials. As shown in Fig. 5d, the addition of tert-butanol (TBA) hardly affected the yield, proving that ·OH radicals are not the main intermediates. Conversely, the introduction of the hole scavenger EDTA-2Na [53] and the electron scavenger $AgNO_3$ both led to a significant decrease in H_2O_2 production, demonstrating that photogenerated holes (h^+) and electrons (e^-) participate in the reaction. Consequently, the h^+ are believed to drive the reaction forward by oxidizing H_2O into dissolved O_2, thereby providing a continuous supply for the ORR. Crucially, after adding p-benzoquinone (BQ), H_2O_2 dropped to an undetectable level, indicating that ·O_2^- is an indispensable ROS for H_2O_2 evolution. To verify this conclusion, in situ electron paramagnetic resonance (EPR) spectroscopy was conducted using DMPO as a spin trap (Fig. 5e). It was found that the DMPO-·O_2^- signal gradually intensified with prolonged irradiation time, confirming the continuous generation of ·O_2^- intermediates via a single-electron reduction process of O_2 during the reaction. To reveal the reaction pathway of the material, in situ diffuse reflectance infrared Fourier transform spectroscopy (in situ DRIFTS) was employed to monitor dynamic reaction intermediates on the surface of 10CdSe/TpBpy (Fig. 5f). Over time, a distinct peak emerged at 1166 cm^{-1}, attributed to the characteristic stretching vibration of ·O_2^-. In addition, the absorption bands at 1210–1240 cm^{-1} and

1355–1405 cm^{-1} also showed a prominent trend, corresponding to the ·OOH and H_2O_2 species bound to the catalyst surface, respectively. To unambiguously trace the oxygen source and conclusively verify the catalytic reaction pathway in the pure-water system, isotope labeling experiments using $^{18}O_2$ were conducted, and the headspace gas was analyzed via gas chromatography-mass spectrometry (GC-MS). As shown in the mass spectrum (Fig. 5g), an emerging signal is observed at $m/z = 36$. This result provides vital support for the generation of H_2O_2 from O_2 over 10CdSe/TpBpy via a two-step single-electron oxygen reduction reaction (ORR) pathway.

3.4. Theoretical calculation

Furthermore, the work functions of both phases were derived from their electrostatic potential distributions. The results showed that the work functions of pure CdSe and pure COF-TpBpy were 4.656 eV and 5.197 eV, respectively (Fig. S11a-b). The lower work function of CdSe implies that its Fermi level (E_f) is higher than that of COF-TpBpy, providing the driving force for the spontaneous transfer of electrons from CdSe to COF-TpBpy. To summarize, following their physical connection under unilluminated conditions, the energetic states of the CdSe curve shift upwards, whereas the corresponding levels of COF-TpBpy shift downwards. This induces a spontaneous migration of negative charges toward the COF-TpBpy boundary to equilibrate their respective Fermi positions, thereby generating an internal electric potential oriented from CdSe to COF-TpBpy. Actuated by this resultant field, light-excited electrons occupying the COF-TpBpy's conduction minimum undergo rapid recombination against holes located within the CdSe valence maximum. This distinct migration pattern flawlessly corroborates the formation of an S-scheme catalytic architecture.

The optimized structural models of CdSe, COF-TpBpy, and COF-TpBpy@CdSe are shown in Fig. 6a. Once the two phases contact to form a heterojunction, charge density difference (CDD) analysis clearly visualizes charge redistribution at the interface (Fig. 6b, S12). Electrons migrate massively from the CdSe side to the COF-TpBpy side, with a calculated transferred electron number as high as 2.34 e. This charge transfer leads to the accumulation of positive charges at the CdSe interface and negative charges at the COF-TpBpy interface, corroborating the existence of an IEF pointing from CdSe to COF-TpBpy at the interface. Subsequently, we simulated the oxygen reduction reaction pathway for photocatalytic H_2O_2 production (Fig. 6c-d). Gibbs free energy calculations indicate that on the composite surface, the process from the adsorption and activation of O_2 molecules to the formation of the *OOH intermediate exhibits significant exothermic properties. Moreover, the critical step of forming *HOOH shows an extremely low energy barrier. From a thermodynamic perspective, this strongly validates the superior intrinsic catalytic activity of the CdSe/TpBpy heterojunction for highly efficient H_2O_2 synthesis under sacrificial-agent-free conditions. Especially, we evaluated the ΔG for O_2 adsorption across three potential sites: the N site on COF-TpBpy (Fig. S13a), the Cd site on CdSe (Fig. S13b), and the interfacial site between Cd and N (Fig. S13c). The adsorption of O_2 at the Cd-N interfacial site exhibits the most negative ΔG, indicating that this intimately coupled junction region serves as the most thermodynamically favorable active center for oxygen activation.

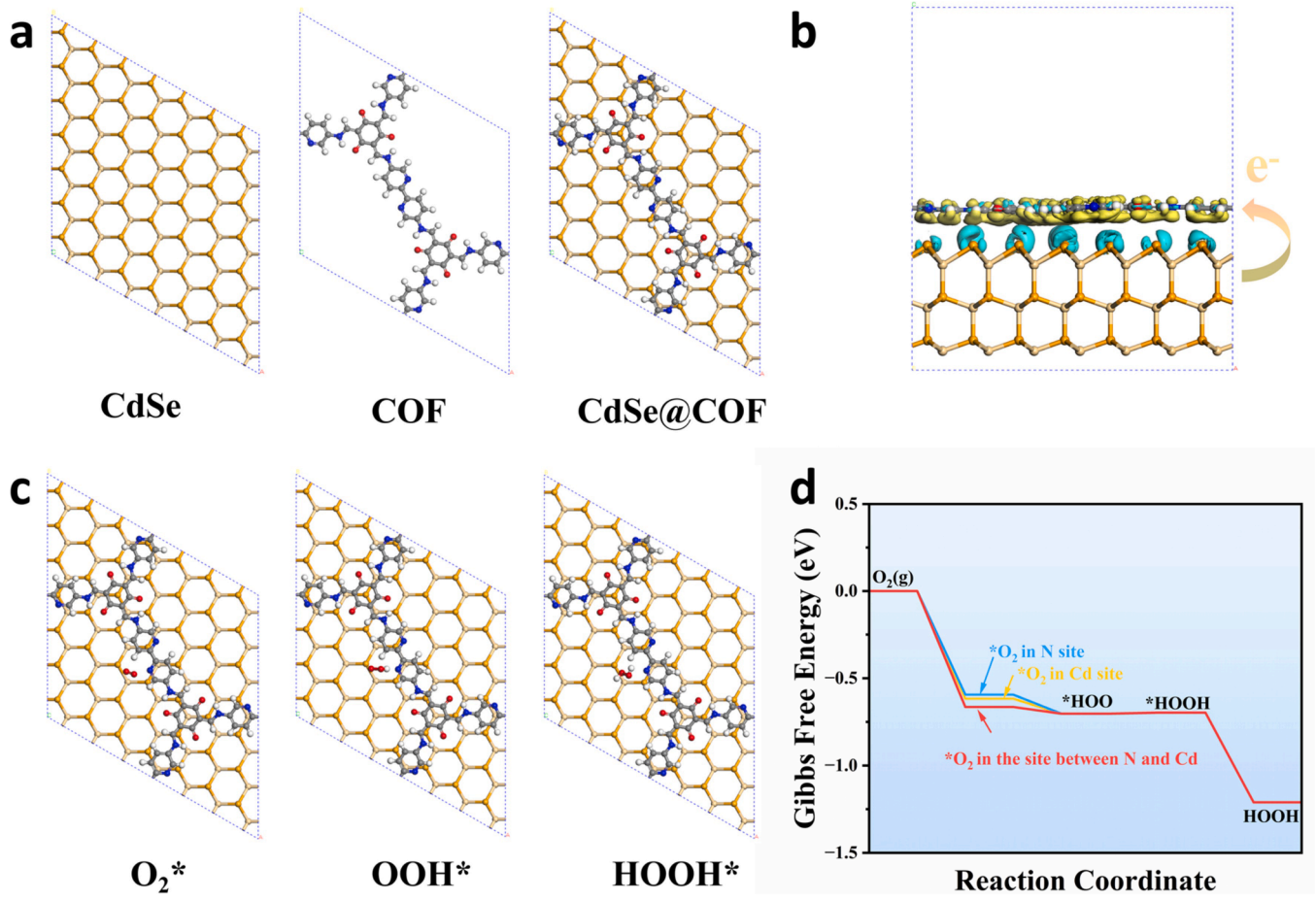

Fig. 6. (a) Structural models of CdSe, COF-TpBpy, and COF-TpBpy@CdSe. (b) Calculated 3D charge density difference (CDD) distribution of COF-TpBpy@CdSe. (c, d) Free energy diagrams of the ORR at the active sites of COF-TpBpy@CdSe.

4. Conclusion

In conclusion, a novel CdSe nanorod/COF-TpBpy S-scheme heterojunction was engineered for efficient, sacrificial-agent-free photocatalytic H_2O_2 generation. The optimized 10CdSe/TpBpy composite exhibited a remarkable H_2O_2 production rate of 4349 $\mu mol \cdot g^{-1} \cdot h^{-1}$, surpassing pure CdSe by 8.3 times. Both experimental evidence and DFT calculations reveal that the work function mismatch induces spontaneous electron flow from CdSe to COF-TpBpy, creating a built-in electric field. Upon irradiation, the synergy of this field and band bending steers an S-scheme charge transfer mechanism, which maximizes the redox capabilities by retaining reductive electrons in CdSe and oxidizing holes in COF-TpBpy. This work offers a promising strategy for green H_2O_2 synthesis and deepens the fundamental understanding of S-scheme heterojunction design for solar-to-chemical conversion.

Declaration of Competing Interest

The authors declare that they have no known competing financial interests or personal relationships that could have appeared to influence the work reported in this paper.

Acknowledgements

This work was funded by the National Key Research and Development Program of China (2021YFA1501404), and the Science and Technology Commission of Shanghai Municipality (2024ZDSYS02).

Appendix A. Supporting information

Supplementary data associated with this article can be found in the online version at doi:10.1016/j.apcatb.2026.127409.

Data availability

Data will be made available on request.

References

[1] B.S. Lane, K. Burgess, Metal-catalyzed epoxidations of alkenes with hydrogen peroxide, Chem. Rev. 103 (7) (2003) 2457–2474.
[2] J. Hu, B. Li, X. Li, et al., Lattice match-enabled covalent heterointerfaces with built-in electric field for efficient hydrogen peroxide photosynthesis, Adv. Mater. 36 (49) (2024) 2412070.
[3] M. Sayed, H. Li, C. Bie, Challenges and prospects of photocatalytic H_2O_2 production, Acta Phys. -Chim. Sin. 41 (9) (2025) 100117.
[4] H. Hou, X. Zeng, X. Zhang, Production of hydrogen peroxide by photocatalytic processes, Angew. Chem. Int. Ed. 59 (40) (2020) 17356–17376.
[5] J.M. Campos-Martin, G. Blanco-Brieva, J.L.G. Fierro, Hydrogen peroxide synthesis: An outlook beyond the anthraquinone process, Angew. Chem. Int. Ed. 45 (42) (2006) 6962–6984.
[6] N. Meng, M.H. Zhou, X.G. Zhang, et al., Construction of proton relay on carbon quantum dots for highly efficient hydrogen peroxide photo-production, Chem. Eng. J. 503 (2025) 15.
[7] Y.N. Zhang, C.S. Pan, G.M. Bian, et al., H_2O_2 generation from O_2 and H_2O on a near-infrared absorbing porphyrin supramolecular photocatalyst, Nat. Energy 8 (4) (2023) 361–371.
[8] J. Qiu, K. Meng, Y. Zhang, et al., COF/In_2S_3 S-scheme photocatalyst with enhanced light absorption and H_2O_2-production activity and fs-TA investigation, Adv. Mater. 36 (24) (2024) 2400288.
[9] H. Gu, H. Zhang, X. Wang, et al., Robust construction of CdSe nanorods@Ti_3C_2 MXene nanosheet for superior photocatalytic H_2 evolution, Appl. Catal. B Environ. 328 (2023) 122537.
[10] C. Wang, Y. Zhao, C. Cheng, et al., S-scheme heterojunction photocatalysts: Mechanism, challenges and opportunities, Coord. Chem. Rev. 521 (2024) 216177.
[11] M. Malhotra, P. Singh, Q.V. Le, et al., Strategic design and mechanistic unveiling of Ni-based S-scheme heterojunctions for efficient CO_2 photoreduction to C1 products: Coordination chemistry, spectroscopic evidence, and future directions, Coord. Chem. Rev. 548 (2026) 32.
[12] F. Xu, F. Zhao, X. Deng, et al., Integrating S-scheme photocatalysis with tandem carbonylation: A green and scalable strategy for CO_2 valorization, Nat. Commun. 16 (1) (2025) 6882.
[13] L. Gao, Y. Huang, J. Meng, et al., Engineering the 1T/2H-$MoSe_2$ phase junction as an S-scheme cocatalyst for boosted photocatalytic hydrogen evolution, J. Environ. Chem. Eng. 14 (2) (2026) 121561.
[14] M. Sayed, K. Qi, X. Wu, et al., Cu-based S-scheme photocatalysts, Chem. Soc. Rev. 54 (10) (2025) 4874–4921.
[15] Y. Bian, K. Dai, Interfacial charge transfer via Zn-N bonds in ZnO/COF heterostructure promotes photocatalytic H_2O_2 generation, Chin. J. Catal. 76 (2025) 1–5.
[16] C. Chen, Z. Wang, J. Zhang, et al., Multi-Energy-State covalent organic framework/sulfur-vacancy-engineered $Mn_{0.2}Cd_{0.8}S$ S-scheme photocatalyst for enhanced light harvesting and H_2O_2 generation, Adv. Mater. 38 (33) (2026) e73326.
[17] J. Lv, H. Chu, C. Shao, et al., Recent advances in graded nanomaterial-based photocatalysts: Principles, designs, and applications, Chin. J. Catal. 78 (2025) 75–99.
[18] Z. Liu, Y. Bian, G. Dawson, et al., Rational constructing of $Zn_{0.5}Cd_{0.5}S$-diethylenetriamine/g-C_3N_4 S-scheme heterojunction with enhanced photocatalytic H_2O_2 production, Chin. Chem. Lett. 36 (9) (2025) 111272.
[19] J. Cheng, B. Cheng, J. Xu, et al., Organic-inorganic S-scheme heterojunction photocatalysts: Design, synthesis, applications, and challenges, eScience 5 (3) (2025).
[20] Y. Zhao, X. Li, D. Xue, et al., Harnessing S-scheme COF/$CdIn_2S_4$ heterojunctions for enhanced photocatalytic performance, J. Colloid Interface Sci. 710 (2026) 140030.
[21] M. Zhou, H. Liu, Y. Zhang, et al., situ synthesis of an S-scheme COF-5@$CsPbBr_3$ heterojunction for efficient photocatalytic CO_2 reduction, Nanoscale 18 (9) (2026) 5023–5032.
[22] H. Ran, X. Liu, L. Ye, et al., Construction of CYANO–COF/$ZnIn_2S_4$ S-scheme heterojunction for boosted photocatalytic hydrogen generation, J. Mater. Sci. & Technol. 234 (2025) 24–30.
[23] I.P. Malashin, D. Daibagya, V. Tynchenko, et al., Exploring temperature-dependent photoluminescence dynamics of colloidal CdSe nanoplatelets using machine learning approach, Sci. Rep. 14 (1) (2024) 14.
[24] J.E. Da Silva, D.V. Freitas, F.L.N. Sousa, et al., Electrosynthesis and characterization of alloyed CdS_xSe_{1-x} ternary quantum dots, J. Alloy. Compd. 969 (2023) 172315.
[25] Z. Tang, Y. Tao, K. Wang, et al., Lattice Mn^{2+} doped CdSe/CdS quantum dots for high-performance photoelectrochemical hydrogen evolution, Nano Energy 113 (2023) 108533.
[26] Y.C. Wei, J.C. Chang, Y.H. Chen, et al., Impact of aspect ratio on charge carrier dynamics and efficiency enhancement in CdSe/CdS dot-in-rod nanostructures for photocatalytic hydrogen evolution, J. Phys. Chem. Lett. 15 (50) (2024) 12425–12434.
[27] Y. Chen, W. Zhong, F. Chen, et al., Photoinduced self-stability mechanism of CdS photocatalyst: The dependence of photocorrosion and H_2-evolution performance, J. Mater. Sci. & Technol. 121 (2022) 19–27.
[28] C. Qin, X. Wu, L. Tang, et al., Dual donor-acceptor covalent organic frameworks for hydrogen peroxide photosynthesis, Nat. Commun. 14 (1) (2023) 5238.
[29] W. Wang, X. Wang, Z.Z. Gao, Wei J. Microenvironmental regulation of covalent organic frameworks for photocatalytic hydrogen peroxide production, Coord. Chem. Rev. 506 (May) (2024), 1.1-1.16.
[30] Z. Chen, J. Wang, M. Hao, et al., Tuning excited state electronic structure and charge transport in covalent organic frameworks for enhanced photocatalytic performance, Nat. Commun. 14 (1) (2023) 1106.
[31] L.J. Gong, L.Y. Liu, S.S. Zhao, et al., Rapid charge transfer in covalent organic framework via through-bond for enhanced photocatalytic CO_2 reduction, Chem. Eng. J. 458 (2023) 9.
[32] H. Li, C.K. Cheng, Z.J. Yang, et al., Encapsulated CdSe/CdS nanorods in double-shelled porous nanocomposites for efficient photocatalytic CO_2 reduction, Nat. Commun. 13 (1) (2022) 11.
[33] S.-Y. Li, S. Meng, X. Zou, et al., Rhenium-functionalized covalent organic framework photocatalyst for efficient CO_2 reduction under visible light, Microporous Mesoporous Mater. 285 (2019) 195–201.
[34] D.B. Shinde, H.B. Aiyappa, M. Bhadra, et al., A mechanochemically synthesized covalent organic framework as a proton-conducting solid electrolyte, J. Mater. Chem. A 4 (7) (2016) 2682–2690.
[35] M. Kou, Y. Wang, Y. Xu, et al., Molecularly engineered covalent organic frameworks for hydrogen peroxide photosynthesis, Angew. Chem. Int. Ed. 61 (19) (2022) e202200413.
[36] J.B. Xue, C.K. Lei, Q.R. Li, et al., Hydrogen-bonded CdSe/PDI with double electric field synergism for enhanced overall water splitting performance, J. Mater. Chem. A 12 (11) (2024) 6582–6591.
[37] Y. Fang, Y. Liu, H. Huang, et al., Design and synthesis of broadband absorption covalent organic framework for efficient artificial photocatalytic amine coupling, Nat. Commun. 15 (1) (2024) 4856.
[38] S.T. Bao, Q.Y. Tan, S.D. Wang, et al., TpBD COF@$ZnIn_2S_4$ nanosheets: A novel S-scheme heterojunction with enhanced photoreactivity for hydrogen production, Appl. Catal. B Environ. Energy 330 (2023) 12.
[39] Y. Zheng, Y. Wang, Y. Chen, et al., 0D/2D S-scheme heterojunction of cadmium selenide and covalent triazine frameworks with enhanced photocatalytic activity for hydrogen evolution, carbon dioxide reduction and terpene dehydrogenation, Mater. Today Chem. 41 (2024) 102324.
[40] Z. Chen, D. Yao, C. Chu, et al., Photocatalytic H_2O_2 production systems: Design strategies and environmental applications, Chem. Eng. J. 451 (2023) 138489.
[41] M. Xu, X. Ruan, X. Zhang, et al., Localized oxygen enrichment in a covalent organic framework-$ZnIn_2S_4$ S-scheme heterojunction enables spatially confined oxygen reduction and boosts photocatalytic H_2O_2 selectivity, Nano Lett. 25 (35) (2025) 13315–13325.

[42] Y. Zhang, J. Qiu, B. Zhu, et al., ZnO/COF S-scheme heterojunction for improved photocatalytic H_2O_2 production performance, Chem. Eng. J. 444 (2022) 136584.
[43] Y. He, J. Zhao, Y.-T. Sham, et al., Efficient hydrogen peroxide photosynthesis over CdS/COF for water disinfection: The S-scheme pathway, oxygen adsorption, and reactor design, ACS Sustain. Chem. & Eng. 11 (49) (2023) 17552–17563.
[44] J. Sahu, S. Mansingh, B.P. Mishra, et al., Compositionally engineered Cd–Mo–Se alloyed QDs toward photocatalytic H_2O_2 production and Cr(VI) reduction with a detailed mechanism and influencing parameters, Dalton Trans. 52 (44) (2023) 16525–16537.
[45] H. He, Z. Wang, J. Zhang, et al., Interface chemical bond enhanced ions intercalated carbon nitride/CdSe-diethylenetriamine S-scheme heterojunction for photocatalytic H_2O_2 synthesis in pure water, Adv. Funct. Mater. 34 (24) (2024) 2315426.
[46] Y. Huang, X. Wang, H. Zhang, et al., Nb_2C MXene quantum dots modulate built-in electric field within heterostructures for efficient solar-to-H_2O_2 conversion from seawater, Appl. Catal. B Environ. Energy 371 (2025) 125262.
[47] J. Sahu, J. Panda, P.P. Sarangi, et al., Boosting the photocatalytic O_2 reduction reaction for H_2O_2 production over CuS nanosheets decorated with CdSe quantum dots, ChemCatChem 17 (10) (2025) e202402147.
[48] L. Zhuo, S. Dong, Y.T. Sham, et al., Internal electric field steering S-scheme charge transfer in $ZnIn_2S_4$/COF boosts H_2O_2 photosynthesis from water and air for sustainable disinfection, npj Clean. Water 8 (1) (2025) 5.
[49] Y. Bian, Z. Wang, M. Du, et al., Strain-amplified interfacial electric field in an S-scheme Cu-TCPP/CdSe heterojunction for efficient photocatalytic H_2O_2 production in pure water, Adv. Funct. Mater. 36 (17) (2026) e19493.
[50] Y. Gao, B. Ge, H. Zhao, et al., Boosting photocatalytic H_2O_2 production via the synergy of protonation and heterojunction in covalent organic frameworks, Langmuir 42 (8) (2026) 6333–6343.
[51] C.J. Wang, Y.P. Yang, F.L. You, et al., Sonochemical accelerated fabrication of $MgIn_2S_4$/COFs S-scheme heterojunction for efficient photocatalytic H_2O_2 production, Ultrason. Sonochem. 124 (2026) 10.
[52] Y.Z. Wu, Y. Chen, D.L. Li, et al., Interface engineering of organic-inorganic heterojunctions with enhanced charge transfer, Appl. Catal. B Environ. Energy 309 (2022) 12.
[53] N. Denisov, J. Yoo, P. Schmuki, Effect of different hole scavengers on the photoelectrochemical properties and photocatalytic hydrogen evolution performance of pristine and Pt-decorated TiO_2 nanotubes, Electrochim. Acta 319 (2019) 61–71.